The THEMIS ESA Plasma Instrument and In-flight Calibration

J.P. McFadden, C.W. Carlson, D. Larson, V. Angelopoulos, M. Ludlam, R. Abiad, B. Elliot

University of California
Space Sciences Laboratory
7 Gauss Way
Berkeley, CA 94720

mcfadden@ssl.berkeley.edu
510-642-9918 office
510-643-8302 fax

The THEMIS ESA Plasma Instrument and In-flight Calibration

Abstract

The THEMIS plasma instrument is designed to measure the ion and electron distribution functions over the energy range from a few eV up to 30 keV for electrons and 25 keV for ions. The instrument consists of a pair of "top hat" electrostatic analyzers with common 180^{o} x 6^{o} fields-of-view that sweep out 4π steradians each 3s spin period. Particles are detected by microchannel plate detectors and binned into six distributions whose energy, angle, and time resolution depend upon instrument mode. The on-board moment processing includes corrections for spacecraft potential. This paper focuses on the ground and in-flight calibrations of the 10 sensors on five spacecraft. Cross-calibrations were facilitated by having all the plasma measurements available with the same resolution and format, along with spacecraft potential and magnetic field measurements in the same data set. Lessons learned from this effort should be useful for future multi-satellite missions.

Keywords
THEMIS, Space Plasma Instrument, Calibrations, Electrostatic Analyzer

Classification System
94.80.+g
06.20.fb
94.30.C-
94.05.-a
07.87.+v

1.0 Introduction

The THEMIS mission was designed to study fundamental processes concerning the nature of magnetospheric substorms, the explosive release of solar wind energy stored in the Earth's magnetotail (Vassilis et al., 2008). To address the substorm problem, THEMIS utilizes five identical spacecraft which are placed in highly-elliptical near-equatorial orbits with apogees of ~14.7 Re for three inner probes, and apogees of ~19.6 and ~31.6 Re for the outer probes. Orbital periods for the probes are 1, 2 and 4 days allowing magnetotail alignment conjunctions once every 4 days as required for substorm timing analysis.

THEMIS was launched on February 15, 2007, into an initial insertion orbit with an apogee near ~21 MLT and shifting to the dayside with the Earth's orbital motion. This orbit required a 7 month coast phase, where the spacecraft were kept in a close configuration to keep orbital parameters optimized for final orbit insertion in the fall of 2007. This close proximity allowed accurate cross-calibration of the plasma instruments as described in section 2 in preparation for the substorm campaign in early 2008. In addition, "First results" papers in this issue are primarily concerned with dayside science investigations. In particular, first results from the plasma sensors, along with other performance issues, can be found in the companion paper, McFadden et al. (2008).

Each THEMIS spacecraft (Harvey et al., 2008) contains a fluxgate magnetometer (Auster et al., 2008), a search-coil magnetometer (Roux, et al., 2008), electric field instrument (Bonnell et al., 2008), solid state telescopes (Larson et al., 2008) and the ESA (Electro-Static Analyzer) plasma instrument described below. These core instruments provide a set of measurements needed to resolve the in-situ dynamics of substorms. The plasma instrument provides detailed ion and electron particle distribution function measurements along with on-board moment calculations. The overall mechanical and electrical design of the THEMIS ESA plasma instrument was directly derived from the FAST Plasma Instrument (Carlson et al., 2001). Below we present a description of the instrument geometry and data products, followed by an in depth discussion of the calibrations. Lessons learned from this calibration effort should be useful for future multi-satellite missions.

1.1 Sensor Description

The THEMIS plasma instrument consists of a pair of top-hat electrostatic analyzers (ESAs) (Carlson et al., 1983) that measure ion and electron energy/charge (E/q). Figure 1 shows a picture and cross-section of the sensors which are packaged together to provide a common field-of-view (FOV). The electron and ion analyzers have $\Delta R/R$ of 0. 0.060 and 0.075, respectively, providing inherent energy resolutions of 15% and 19%. The sensors are logarithmically swept in energy from ~32 keV for electrons, and ~25 keV for ions, down to a few eV. Nominal operations have 32 sweeps per spin, with 32 energy samples per sweep, resulting in a measurement resolution with $\Delta E/E$~35%. Particle events are registered by microchannel plate (MCP) detectors.

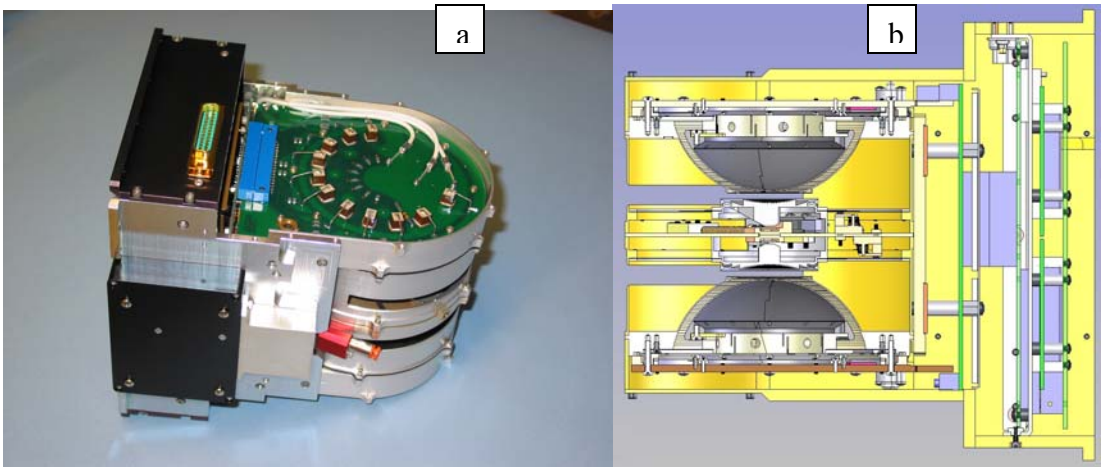

Figure 1: The THEMIS ion and electron Electrostatic Analyzers (ESAs) are packaged together to provide a common field of view. a) ESA with the anode cover removed reveals coupling capacitors. The LVPS (black) is mounted on the side and the nitrogen purge inlet (red) is exposed. b) Analyzer cutaway shows the common aperture mechanism and electronics packaging.

Both sensors have a 180^o x 6^o FOV (FWHM), with the 6^o rotating with the spacecraft to provide 4π steradian coverage each spin. 32 sweeps per spin provides 11.25^o resolution in rotation phase (φ). The electron sensor has 8 anodes giving 22.5^o resolution in the polar angle (θ), while the ion sensor has 16 anodes with up to 5.625^o resolution. The high angular resolution anodes in the ion sensor are concentrated at the spin plane to resolve solar wind ions. The ion sensor can also be operated in a double-sweep mode (64 sweeps/spin) to provide a similar 5.625^o angular resolution in rotation phase.

Figure 2 illustrates the ESA plasma instrument's modular design which allows subassemblies to be constructed and tested separately. Figure 2a shows the MCP (red) detectors and mounting hardware that attach to the anode. Spring fingers on both the inner and outer edges of the MCP annulus distribute the force providing uniform clamping that can withstand >100Gs of acceleration. This subassembly allows MCP testing and characterization prior to sensor assembly. The tab on the lower right corner of the anode is the interface to the purge tube that that supplies filtered dry nitrogen during storage. Figure 2b reveals an analyzer design that maintains its concentricity to ~15 um under normal assembly. Although the hemisphere alignment is controlled by three interfaces, the flexible insulator that supports the inner hemisphere is self-centering producing an alignment equivalent to the tolerance at the outer mounting plate interface. The outer hemisphere was serrated and all internal surfaces were blackened with ebanol-C to reduce scattered sunlight from reaching the detectors. (Ebanol-C is found to reduce scattered sunlight by at least a factor of 10 over gold-black, which was used on FAST.) Figure 2c shows the combined anode, analyzer, outer aperture, and the top-hat. The top-hat is supported by a torsion spring and contains a conductive gasket that seals against the outer hemisphere during launch to prevent contamination. Figure 2d shows the release plate mechanism that pushes both ion and electron sensor top-hats into closed positions against their outer hemispheres. The reset-able, SMA-actuator release mechanism was developed for the THEMIS program to simplify sensor refurbishment during ground testing, replacing a melt-wire design used for the FAST mission. The release mechanism

also acts as a poppet valve during nitrogen purge and rocket ascent, preventing over-pressure by venting gas at the top-hat.

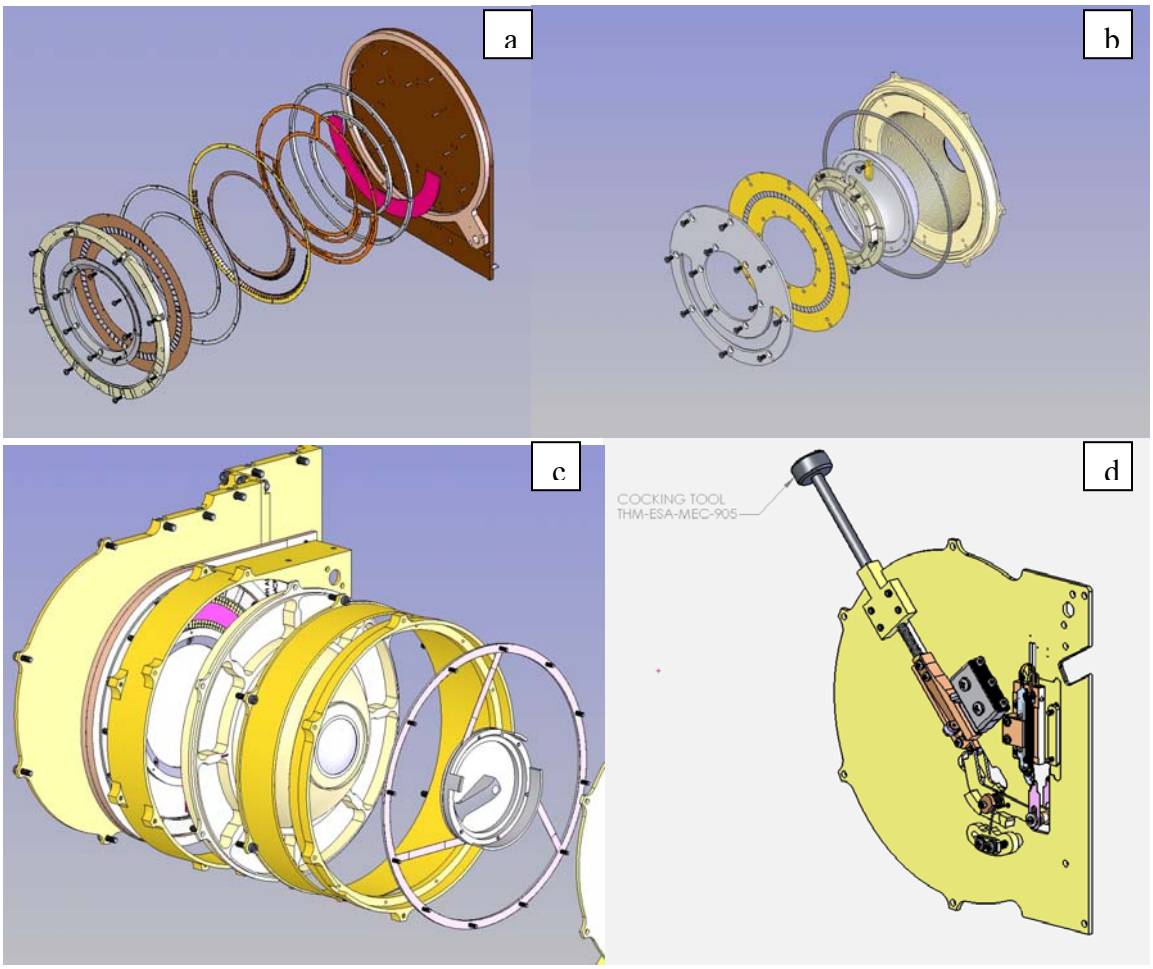

Figure 2: a) THEMIS detector-anode module, b) analyzer module, c) sensor subassembly, and d) the aperture release plate mechanism with SMA actuator. The modular mechanical design allowed subsystem assembly and testing to proceed in parallel for the 10 ESA sensors.

The modular design also extends to the ESA electronics as illustrated in Figure 3. The instrument simplifies assembly by eliminating most of the harnessing by coordinating the mechanical and electrical designs. Figure 3a and 3b show the preamplifier board which contains 24 Amptek A121 preampliers for both sensors. This board uses a single FPGA to implement counters and a command decoder that controls its test pulser and the preamplifier gains. Separate high voltages (HV) boards are used for electron and ion sensors, each board (Figure 3c) containing a raw sweep supply and MCP supply for a single sensor. The HV boards mount to a common mechanical frame (Figure 3d) that also supports the Interface-Sweep (IS) board (Figure 3e) and a small mother board (Figure 3d) that provides an electrical interface between the IS and HV boards. The IS board contains opto-coupler (Amptek HV601) circuits for analyzer HV sweeps, in addition to providing FPGA control voltages for the sweeps and the HV boards. The combined electron-ion instrument requires two +28V power lines, one for low voltage (LV) and one for HV. Figure 3f shows the LV power supply which mounts to the side of the ESA instrument.

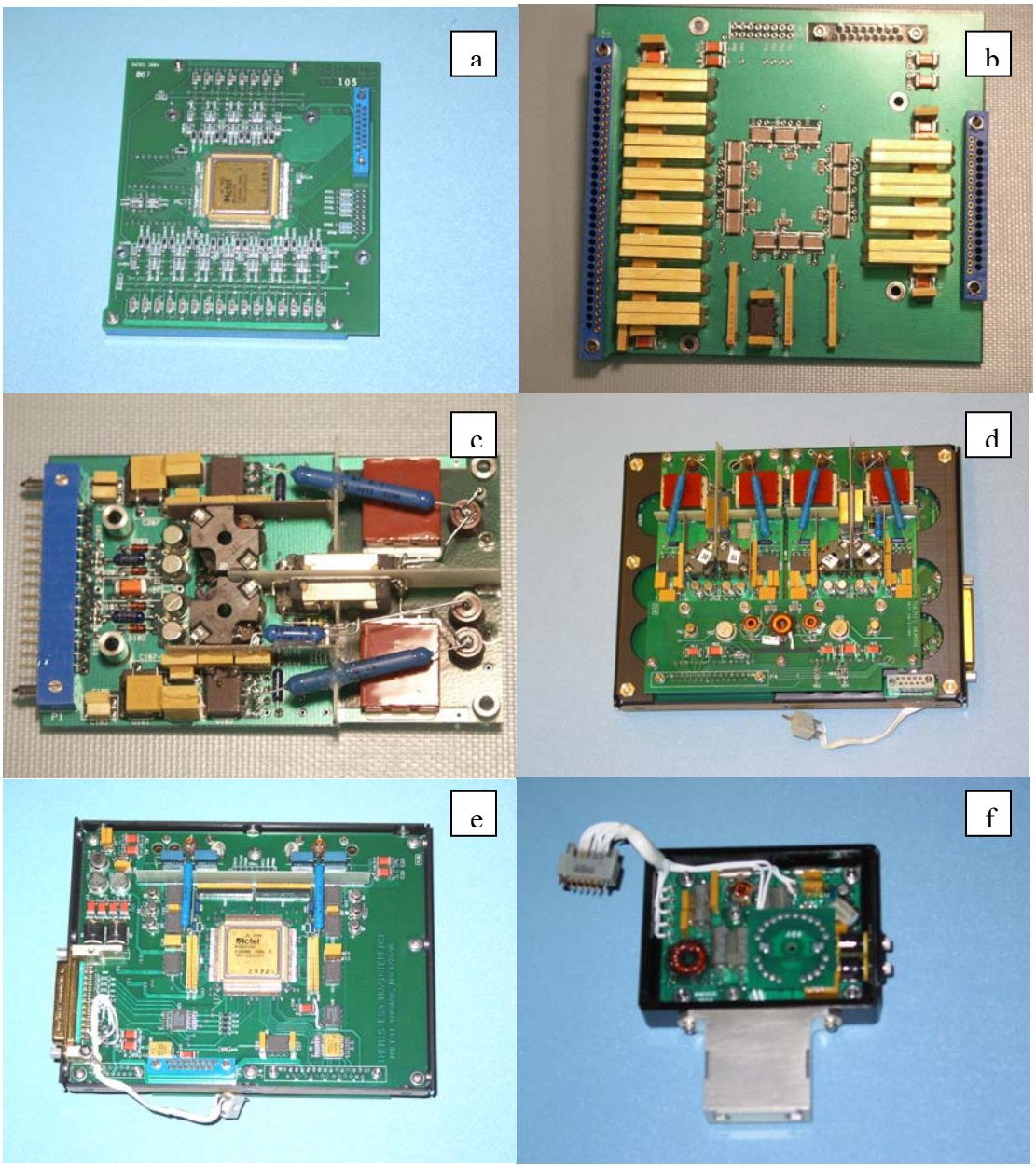

Figure 3: The THEMIS ESA electronics consists of a) the preamplifier board, b) the high voltage power supplies and mother board, c) the interface and sweep control board, and d) the low voltage power supply. The modular mechanical-electrical design minimized harnessing, allowing quick assembly and disassembly of the instruments.

The ESA interfaces to the Instrument Data Processing Unit or IDPU (Taylor et al., 2008) which provides power, control, and data interfaces. Figure 4 shows a block diagram of the ESA. MCP detectors in chevron configuration are voltage biased at ~2 kV to amplify input events to ~10^6 e-, approximately -160 fC. Amptek A121 preamplifiers are used to detect output charge pulses and have programmable gain to facilitate testing. For nominal operation the preamplifier thresholds are set at ~35 fC. Events are recorded by counters

which are read out 1024 times per spin. The ESA electronics include a programmable test pulse generator to provide electronic stimulation when high voltage is off. The rate of this stimulation can be slaved to the analyzer sweep control to confirm internal timing.

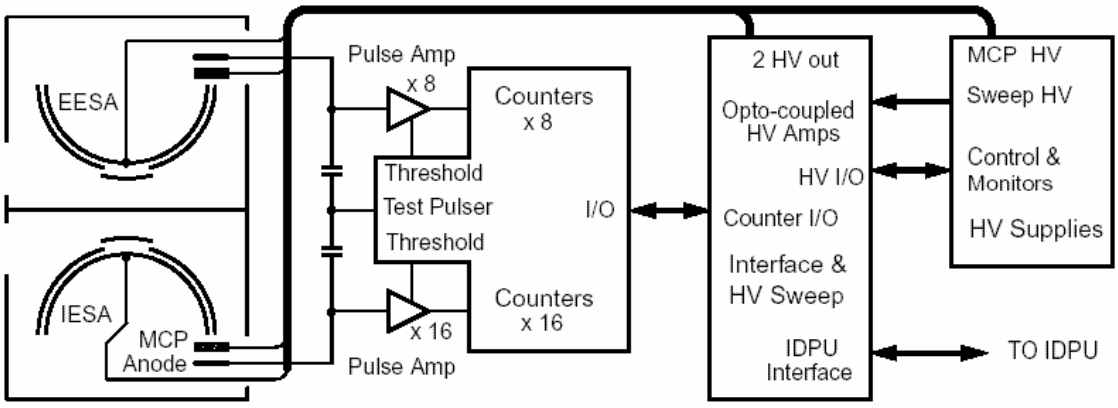

Figure 4: THEMIS ESA block diagram

As mentioned above, the ESA contains four separate high voltage power supplies (HVPS), two for MCPs and two for the ion and electron energy sweeps. All HVPS are separately controlled by the IDPU to allow independent operation of both sensors. The sweep supplies produce a 5 kV maximum output (-5kV for ions), that is used as a raw input to an opto-coupler circuit that provides voltage to the inner hemispheres. The hemispheres are swept from high voltage to low voltage in ~100 ms, with ~1 ms required for the high voltage to retrace to its starting value. The energy sweep is synchronized to the 1024 pulse/spin input clock that also controls counter readout.

1.2 ESA Modes and Data Products

ESA data are collected and formatted by the ETC board in the IDPU into several data products: survey packets, burst packets, reduced packets, and moment packets. Each sensor has separate packets, except for moment packets which are made by combining data from both ESAs and the Solid State Telescopes (SSTs) (Larson et al., 2008). The format of each data product is programmable and may change with time depending on the "Spacecraft-Mode", the location within the magnetosphere, or when new "instrument-modes" are uploaded to the satellites. Below we describe data products generated by the nominal "magnetospheric mode" used for the majority of the first nine months of the mission.

"Survey packets" are a low-time-resolution data product useful for large scale "surveys" of THEMIS data. They generally maintain the full 32 energies sampled, but have a reduced 88 solid-angle map as illustrated in Figure 5. Survey data are 1-spin snapshots of the plasma with a measurement cadence of either 32 spins (in "Fast-Survey Spacecraft-Mode") or 128 spins ("Slow-Survey Spacecraft-Mode"). These high energy-angle resolution measurements are the primary data product used for the in-flight calibration effort described below. Survey packets are used to generate summary plots, to validate the on-board plasma moment computations, and to provide detailed distribution functions

in all regions of the magnetosphere. Survey data are particularly helpful for the identification of unique features, such as counter-streaming field-aligned beams, that may not be easily identified from other data products such as moments.

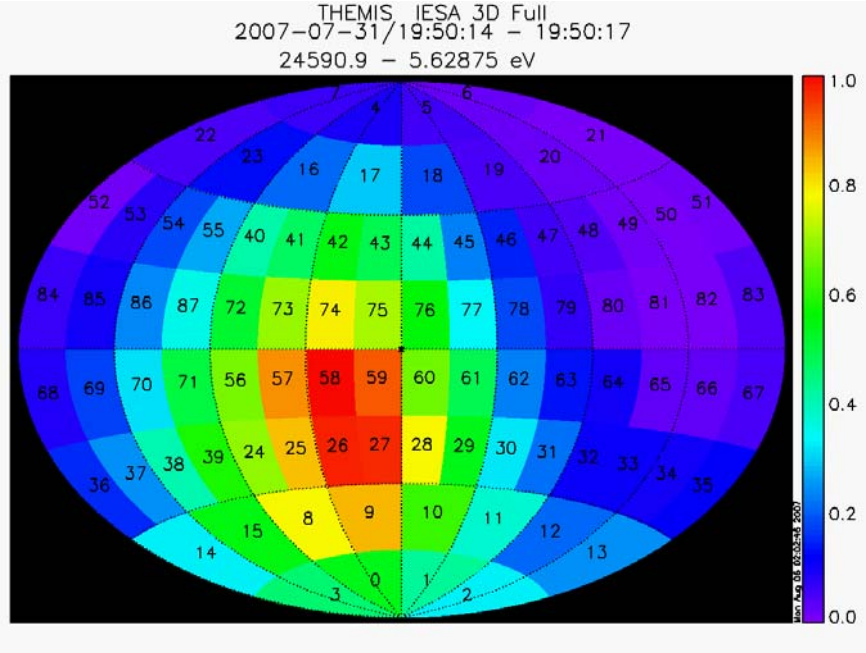

Figure 5: Typical 88 solid-angle map used for collecting ESA data into survey and burst data packets.

"Burst packets" contain high-resolution 3-D plasma distribution functions with spin-period time resolution. Due to telemetry limitations, burst packets are generally limited to several, five-minute-intervals each orbit. Burst packet format is usually the same as survey packet format, with 32 energies and 88 solid angles. The selected time intervals are chosen by ground command or by on-board triggers as discussed in Vassilis et al. (2008). Burst data provides the high resolution measurements needed to resolve boundary crossings such as the magnetotail neutral sheet, plasma sheet boundary layer, magnetopause, and bow shock.

"Reduced packets" are 1-spin-resolution plasma distributions sampled continuously, but with limited solid-angle and/or energy coverage. When in Slow-Survey mode, reduced packets are generally composed of 32-energy, omni-directional spectra which allow energy-time spectrograms with the same cadence as on-board moment data. In Fast-Survey mode, the nominal ion reduced packet consists of a 24-energy, 50-solid-angle distribution, while the electron reduced packet is a 32-energy, 6-solid-angle distribution (see Figure 6). These Fast-Survey mode formats were chosen to maintain enough angular information so that plasma moments could be computed and so features of the distribution, such as field-aligned beams, could be deduced. When combined with on-board spin-resolution moment data, reduced data allows high-time resolution science investigations to be conducted on data gathered throughout the orbit.

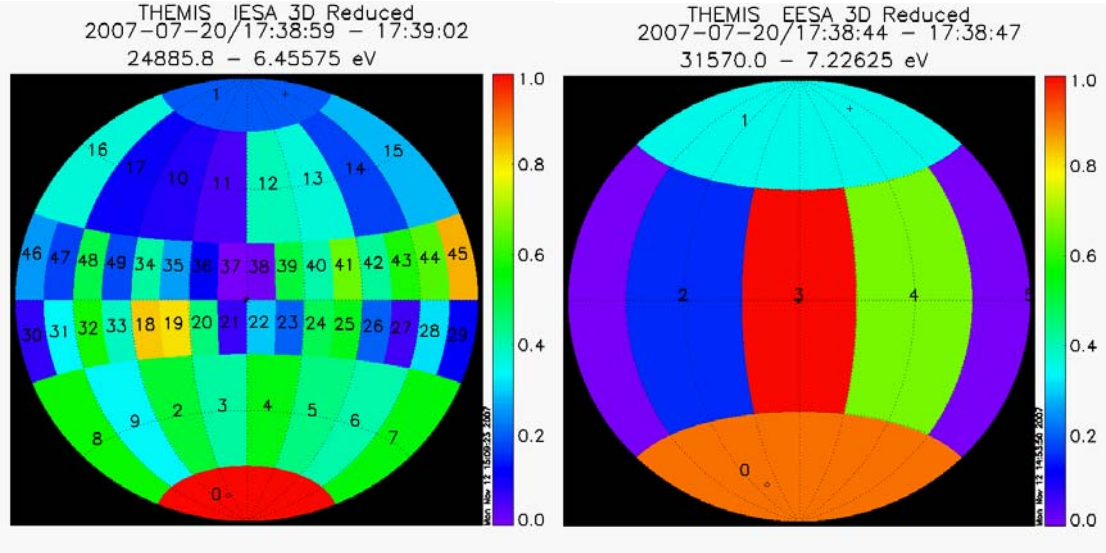

Figure 6: Typical ion (left) and electron (right) solid angle maps showing angle bin number for reduced data packets during fast survey magnetospheric mode. Reduced data are produced at spin resolution and maintain 32 energies for electrons and 24 energies for ions. The 50 solid angles for the ions are adequate for accurate velocity moments except during narrow beams along the spin axis. The 6 solid angles for electrons are adequate to identify anisotropies such as counter-streaming electrons.

"Moment packets" include spin-resolution on-board computations of the plasma density, three components of flux (velocity=flux/density), six components of the pressure tensor, and 3 components of heat flux. Moment packets contain calculations of the ion and electron bulk-plasma moments determined from the ESAs, and the SST high-energy (>30 keV) partial moments which can be especially important for determining the total pressure. THEMIS moment calculations are unique in that THEMIS is the first mission to include corrections for spacecraft charging in the calculations. Spacecraft potential, as measured by the EFI instrument (Bonnell et al., 2008), is used to correctly shift the energies of particles in the moment computations. In particular this correction eliminates photo-electrons which often contaminate electron plasma measurements. Moment computations also include weighting factors to correct for energy and angle sensor efficiency which were uploaded after the in-flight calibration effort.

1.3 Ground Testing and Calibrations

In addition to standard functional tests, ground testing of the ESA sensors included several subsystem optimizations prior to assembly and calibration. Before loading into flight boards, A121 preamplifiers were individually tested for response including threshold, output pulse length and dead time to assure nearly identical characteristics for all amplifiers. Opto-coupler high voltage sweep electronics were tuned to provide near zero offset at the lowest DAC control setting (actual voltage offsets were <10 mV on a 4 kV output), to provide nearly identical (~1%) high voltage control gain, and to have rapid settling (~1-2 ms) with no overshoot during high voltage retrace. MCP detectors were matched for current and selected for low background rates and gain uniformity. After sensor assembly, calibrations were performed in high vacuum ($<10^{-6}$ Torr) and included background noise sensitivity, MCP background rates, MCP pulse height distribution

tests, energy-angle characterization, concentricity tests, relative sensitivity characterization, and sweep mode testing.

MCP tests within the analyzer assembly showed background rates 10 to 100 times higher then those observed during subassembly testing with MCPs exposed to the chamber. After several subsystem and system level checks, it was recognized that the higher background resulted from higher pressure at the MCPs which were buried deep in a newly assembled instrument. Internal instrument out gassing, and its associated higher pressure, was the source of higher background rates. By allowing more time in high vacuum prior to testing, and by scrubbing the MCPs prior to the beginning of calibration testing, background rates were reduced to relatively low levels that did not impact calibrations. Similar high background rates were observed on some sensors during thermal vacuum testing at the spacecraft level at UCB, with background seen to correlate with chamber pressure and to decrease with time. Spacecraft level Integration and Test (I&T) at JPL, with higher vacuum during the HV tests, showed expected background rates of ~1/s-cm^2. In-flight data have similar low background rates.

Figure 7 shows the energy-angle calibration for the electron sensor on THC. The inner hemisphere voltage is kept constant while the beam energy and elevation angle are adjusted. The average of this response over elevation angle provides a characteristic energy curve and determines the analyzer energy constant (average energy divided by hemisphere voltage). When the response is averaged over energy, the test provides a measure of the out-of-plane angular acceptance of the instrument. These tests were compared with simulations to confirm proper analyzer operation. Energy-angle tests are performed at three different rotation angles and the instrument's energy calibration is determined from the average energy constant. No significant differences in the energy constant with look direction were found.

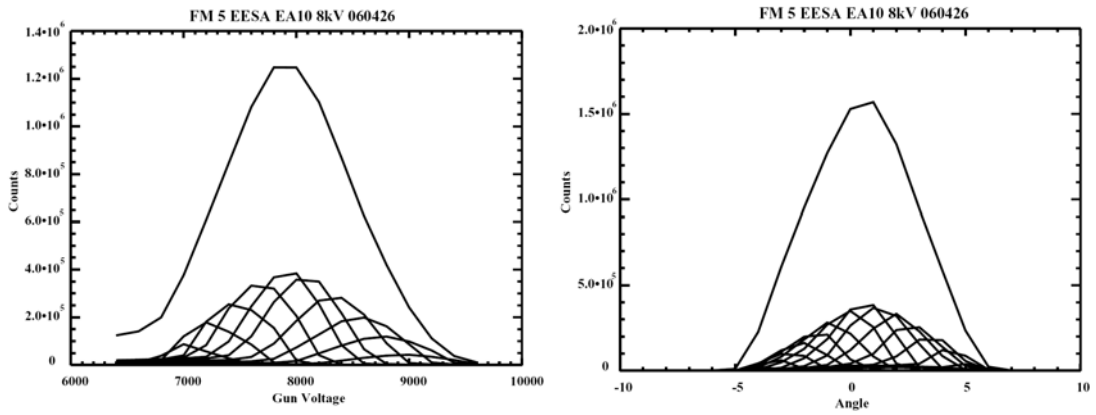

Figure 7: Average energy response (left) and average elevation angle response (right) of the THEMIS electron. The lower curves are energy (angle) response at a single angle (energy). The analyzer energy constant is determined from the curve on the left.

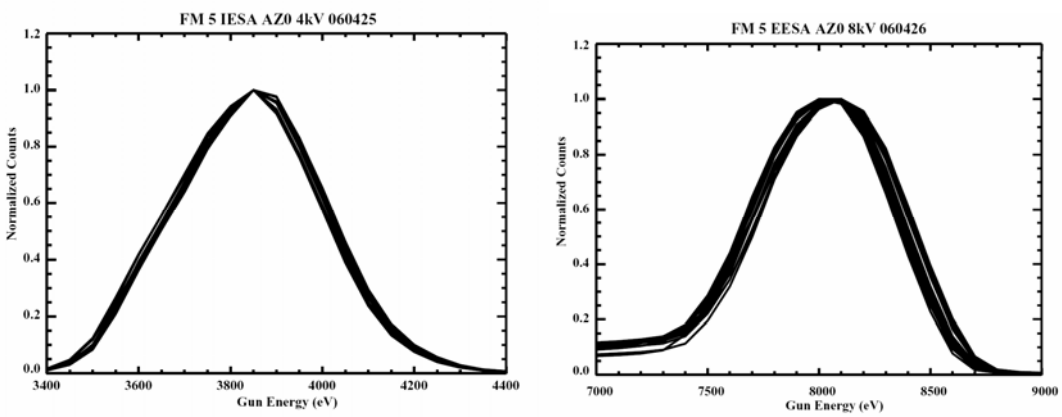

Figure 8: Energy response curve at 0 degree elevation angle for the beam at 15^o increments around the 180^o field of view. Variations indicate about 1% variation in the energy constant with look direction.

One of the most important tests is for concentricity of the analyzer's hemispheres. If the hemispheres are not concentric, the energy of measured particles will be a function of its 180^o FOV, which will complicate data presentation and in-flight calibrations. Although the energy-angle test described above can often identify hemisphere misalignment, a faster test uses a single elevation angle for the beam and sweeps beam energy at a dozen different look directions. Figure 8 shows examples of analyzer concentricity tests for the electron and ion sensors on THC. All THEMIS ESAs were found to have good concentricity with about 1% or less variation in energy with look direction. This accuracy corresponds to a misalignment of hemispheres of ~15 um.

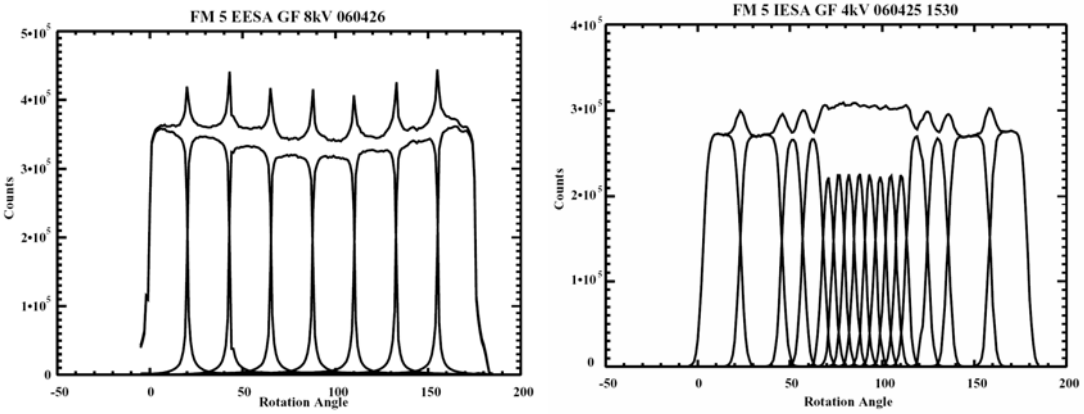

Figure 9: Azimuthal response of the electron (left) and ion (right) sensors on THC to a parallel beam at 0^o elevation angle reveal the 8 anode and 16 anode patterns for the two sensors. A small amount of particle double counting can be seen as enhanced response at the borders between anodes.

Figure 9 shows results from relative sensitivity tests performed on the THEMIS ESAs. For this test the sensor and the beam are optimized for beam throughput and the analyzer is rotated about the symmetry axis. For a parallel beam, the response will be roughly flat, revealing any large asymmetry in the assembly. The ~10% variations in response with look direction are normal and result from a combination of detector bias angle (Gao et al., 1984) and double counting of events at anode boundaries. This test was used early in the

THEMIS calibrations to identify a problem with an aperture opening mechanism. A ~40% variation in sensitivity with rotation was observed on two sensors that simultaneously showed little variation in concentricity. This indicated the top-hat was not seating properly. Careful examination revealed the seating problem which was barely visible to the eye with back lighting to expose a small gap. A clearance problem was identified and the problem was fixed on all sensors. Although these tests provide a preliminary estimate of the uniformity of response, relative sensitivity is much better quantified during in-flight calibrations discussed in section 2.4.

Additional ground calibrations were performed to assure proper operation of the sensor in flight configuration. These included tests of nominal sweeping modes with a beam source and full spacecraft level testing of flight data packaging. However, absolute sensitivity of the sensors and relative efficiency of the detectors with energy were not calibrated due to lack of stable calibrated beams. Instead both these tests are included in the in-flight calibration effort described in sections 2.2, 2.5 and 2.6.

2.0 In-flight ESA Calibrations

The THEMIS and Cluster missions are the only multi-spacecraft missions where four or more satellites have been kept in close proximity allowing detailed cross-calibration efforts between instruments. Unlike the Cluster mission where the electron and ion plasma measurements originated from separate groups and where data products differed in both time and angular resolution, THEMIS offers the advantage of having all the plasma measurements available with the same resolution and format. Furthermore, since all the THEMIS data are distributed as a single data set, spacecraft potential (Bonnell et al., 2008) and magnetic field (Auster et al., 2008) measurements are instantly available in raw or processed form for use in the cross-calibration efforts. This advantage has allowed a detailed cross-calibration effort to be performed in a rather short period of a few months early in the mission. Lessons learned from this effort should be useful for future multi-satellite missions.

The in-flight calibration of the THEMIS electron and ion plasma instruments required inputs from several other instruments including spacecraft potential measurements supplied by EFI, magnetic field measurements supplied by FGM, and spacecraft attitude and timing information supplied by the Mission Operations Center at Berkeley. These inputs were crucial for proper interpretation of the measurements and for confirmation that the sensor operation was nominal. In addition, ESA data were used for in-flight calibration of the EFI and SST instruments as described by Bonnell et al. (2008) and Larson et al. (2008), respectively.

The following sections describe the methodology used for the ESA in-flight calibrations, along with the basic rational for each analysis. Part of this process was the identification of data collection times where known properties of the plasma, such as charge neutrality and gyrotropy, could be used to identify small variations in the sensor response. During this calibration effort, unexpected variations in the ratio Ni/Ne were discovered for several orbits. This led to an investigation of sensor efficiency as a function of energy and the discovery of an unexpected variation in analyzer sensitivity due to leakage fields through the analyzer's exit grids. In addition, the absolute sensitivity calibrations required the use of solar wind data from the Wind spacecraft. Lastly, the ESA calibration effort is not a one-time process. Maintaining accurate calibrations will require continuous monitoring of the detector gain with regular bias voltage adjustments, along with repeated iterations of the techniques described below.

2.1 Spacecraft potential corrections

In order to cross-calibrate sensors using density as a measure of sensitivity, one must include corrections for spacecraft charging. This is especially important for the electron density calculation where inclusion of spacecraft photoelectrons can result in large errors to the density. The electric field experiment (Bonnell et al., 2008) provides a proxy for the spacecraft-to-plasma potential by measuring the potential of Langmuir probes relative to the spacecraft. With a proper bias current to the probes (roughly 25% to 50% of the probe photoemission current) the probe should float within about a volt of the "local"

plasma potential. There are several caveats here. First, the probe and spacecraft must be in sunlight to obtain good current balance between photoemission and plasma collection. Second, by "local" potential, we mean local plasma potential adjacent to the probe. This potential differs from the plasma potential we wish to use as a reference for the spacecraft since the spacecraft, the antenna, and their photoelectrons all perturb to "local" plasma environment. To account for this difference, we introduce a potential "scale factor" that corrects the measured "local" potential to actual plasma potential at large distances from the spacecraft. This "scale factor" is a function of spacecraft potential (or plasma and photoelectron distributions), complicating the calculation. Third, the difference potential between the probe and "local" plasma can vary from near zero in high density plasmas to about two volts in low density plasmas. This potential "offset" also depends on bias current applied to the probe. So like the "scale factor", the "offset" potential varies with spacecraft potential (or plasma and photoelectron distributions). Therefore, calculating the spacecraft potential to be applied to a particle distribution is non-trivial since the measured probe potential depends upon changing parameters such as probe bias current and the plasma distribution.

For THEMIS, the spacecraft potential, Φ_{sc}, is estimated with the following equation.

$$\Phi_{sc} = -A\,(\Phi_{probe} + \Phi_{offset}) \qquad \text{equation 1}$$

where A is a near unity "scale factor", Φ_{probe} is the average radial-probe-to-spacecraft potential, and Φ_{offset} is the potential "offset". Axial-probes are not used in the estimate. Current software sets Φ_{probe} to the spin-averaged potential of two or four radial Langmuir probes, and treats A and Φ_{offset} as constants over an interval with default values of A=1.15 and Φ_{offset}=1.0 V, respectively. These values were determined empirically from spacecraft THC early in the calibration effort by comparisons of calculated electron and ion densities as a function of A and Φ_{offset}. This choice of parameters generally prevents spacecraft photoelectrons from being included in the electron density calculations. Both numbers are consistent with those estimated from previous missions (private communication, F. Mozer) or from THEMIS EFI modeling (private communication, C. Cully).

The need for a "scaling factor" is illustrated in Figure 10. The two electron peaks at 15 eV and 28 eV are the result of photoelectrons emitted from the axial and radial probes, respectively. The vertical line indicates the spacecraft potential determined from equation 1 using the default values for the potential scale factor and offset. At the ~2 m distance of the axial probes, the local plasma potential is about half the spacecraft potential relative to the distant plasma. Since the axial probe comes to equilibrium with the local plasma, its photoelectrons only gain ~$0.5e\Phi_{sc}$ before reaching the plasma sensor. In contrast, the plasma near the radial probes (~20 and ~24 m distance) is at a potential much closer to the distant plasma potential resulting in a spectral peak at energy $E \approx 0.87e\Phi_{sc}$.

In plasma regimes where the bulk of the electrons and ions have energies larger than $e\Phi_{sc}$, plasma moment calculations are not be very sensitive to small errors in the estimated Φ_{sc} as long as Φ_{sc} is large enough to eliminate spacecraft photoelectrons.

However, within the magnetosphere there is often a cold electron component with a sizeable density. This is especially true within the plasmasphere or within plasmaspheric plumes where cold plasma dominates. These cold electrons appear at energies ~$e\Phi_{sc}$ and are difficult to separate from spacecraft or Langmuir probe photoelectrons. In addition, these cold electrons reduce the Debye length, resulting in "scale factors" close to one and Langmuir probes that float very close to plasma potential. For THEMIS data, which generally have energy bins such that $\Delta E/E \sim 0.35$, it may be impossible to separate these cold plasma electrons from the Langmuir probe photoelectrons. Data with these problems were avoided in the in-flight calibration effort.

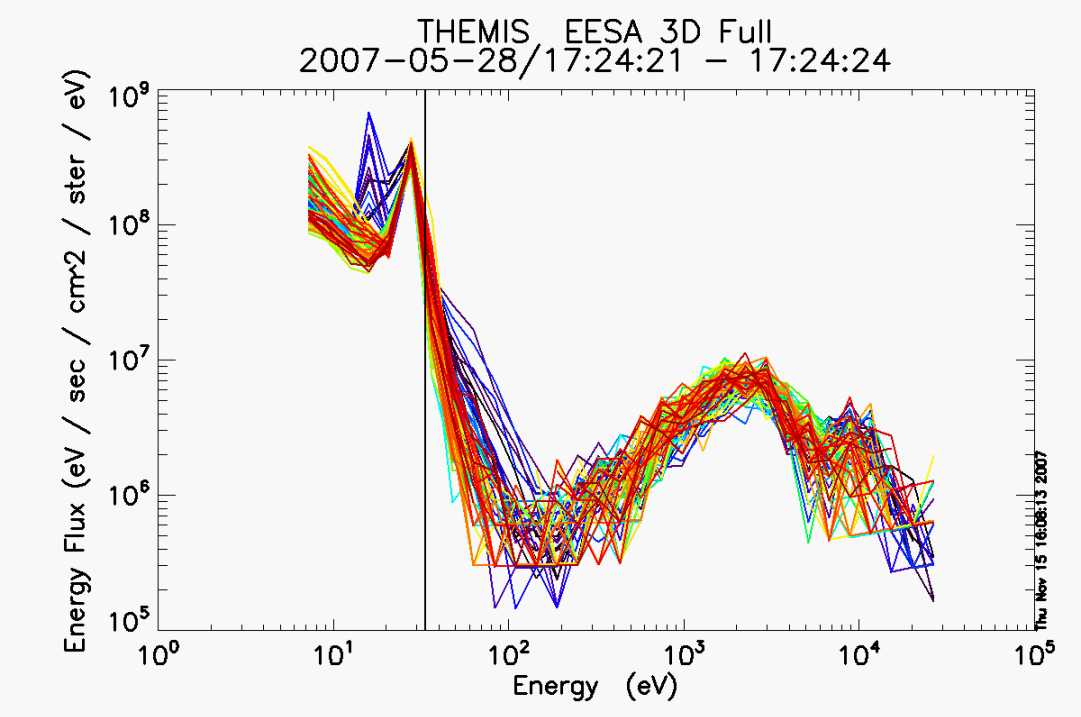

Figure 10: Electron spectra from THC in a low density (n_e~0.2) magnetospheric plasma. Each of the 88 solid angle bins are plotted separately. The line indicates the inferred spacecraft potential using equation 1. The peaks at 15 eV and 28 eV are due photoelectrons from the axial and radial Langmuir probes, respectively. Spacecraft photoelectrons dominate most solid angle bins below 21 eV. Field-aligned electrons are resolved between 40 eV and 150 eV (blue-black), and isotropic hot plasma is observed at higher energies.

THA and THB spacecraft did not have Langmuir probes deployed during the first eight months of the mission and therefore made no in situ potential measurements. To perform cross-calibrations of plasma sensors between spacecraft, it was essential to correct for spacecraft charging. Therefore we developed an empirical method to estimate the spacecraft potential on THA and THB based on the potential of the near-by THD. It was not adequate to assume the same potential as THD since the bias currents applied to the Langmuir probes have a significant affect on spacecraft potential. To develop an empirical relationship between spacecraft, we used data from the EFI bias sweeps (Bonnell et al., 2008) to estimate the change of spacecraft potential as a pair of Langmuir probes were cycled on/off. A perpendicular probe pair was then used to measure the

change in potential. The measurements showed a linear relationship between spacecraft potential with and without bias current applied.

$$\Phi_{no\text{-}bias} = 0.7\Phi_{bias}+0.5, \quad \text{Equation 2}$$

where Φ_{bias} and $\Phi_{no\text{-}bias}$ are difference potentials between the spacecraft and a perpendicular probe pair in volts, with bias current to a radial-probe pair cycled on and off, respectively. In addition, the axial-booms were found to produce a ~0.3 V shift in spacecraft potential. Not enough samples were obtained to determine any dependence of this shift on Φ_{bias}. Combining the above measured differences with equation 1, we estimated the spacecraft-to-plasma potential on THA and THB as

$$\Phi_{THA} \text{ or } \Phi_{THB} = 0.49\Phi_{THD}+1.22, \quad \text{Equation 3}$$

where Φ_{THD} is determined from Equation 1.

The above estimated potentials were used for some of intervals in the cross calibration effort described in section 2.5. However, the EFI operating voltages on the usher and guard surfaces (see Bonnell et al., 2008 for the antenna geometry) were changed -8V to +4V relative to the Langmuir probe surface on June 22, 2007. This reduced spacecraft charging and changed the 0.49 scale factor determined above. To recover an equivalent formula to Equation 3, we performed empirical comparisons between electron spectra and calculated densities, varying the scaling factor to get the best agreement. These comparisons resulted in Equation 4 which should be valid June 23 and September 10, 2007.

$$\Phi_{THA} \text{ or } \Phi_{THB} = 0.8\Phi_{THD}, \quad \text{Equation 4}$$

For most of the in-flight calibration effort discussed below, we selected periods where errors in our estimated spacecraft potential would have minimal effect on the calibration result. During the course of this effort, we observed additional aspects of the dependence of spacecraft potential on the plasma that were not included in this in-flight calibration but are worth noting for future data analysis efforts. First, the probe-to-spacecraft potentials on different "identical" spacecraft in the same environment were not identical and could differ by ~5% at potentials of ~6-8 V. Smaller differences were observed at lower potentials. Although this error is not large, it could cause ~5% difference in estimated plasma density in the solar wind. Second, the ratio of potentials on different spacecraft as the environment changed was not a constant, indicating this was not just a simple difference in a constant "scale factor". These results indicate that for very precise estimates of density, equation 1 will require a different "scale factor" and "offset potential" for each spacecraft and that these parameters likely have a weak functional dependence on potential. For missions such as MMS, where resolving small differences between spacecraft is essential, in-flight calibration efforts must be planned to quantify these small differences.

2.2 Energy-dependent efficiency corrections

Microchannel plate (MCP) detectors are known to vary in efficiency with the incident particle energy (Goruganthu and Wilson, 1984; Straub et al., 1999) and with the incident particle angle relative to the microchannel bias angle (Gao et al., 1984). For THEMIS ESAs, the bias angle of the plates was oriented so that average variations of incident angle around the MCPs is minimized and these efficiency variations are included in "relative efficiency calibration with look direction" discussed later. For energy dependent efficiencies, we initially adopted values published in the literature for electron and ions as shown in Figure 11a and 11b.

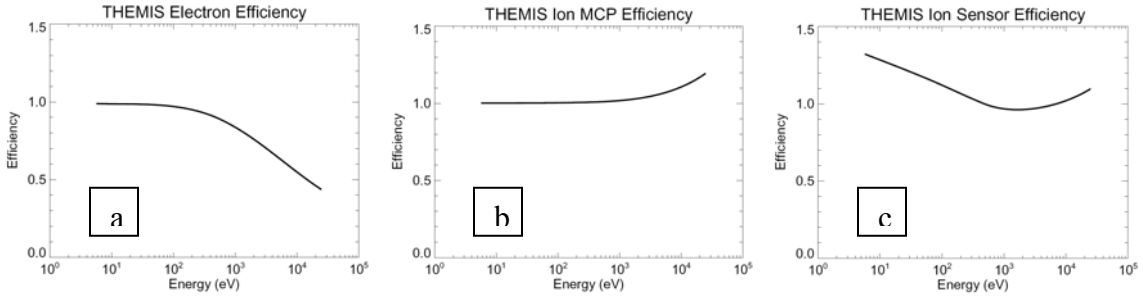

Figure 11: a) Electron MCP energy efficiency adapted from Goruganthu and Wilson, (1984), b) ion MCP energy efficiency adapted from Funsten (private communication), and c) ion sensor energy efficiency (analyzer+MCP) which includes leakage fields at the exit grids that increase analyzer geometric factor over the ideal analyzer. See text for discussion.

However, early in the calibration effort it was discovered that the calculated ratio of electron and ion density appeared to depend upon ion energy. In particular the presence of low energy (<100 eV) ions seemed to increase the Ni/Ne ratio. Not knowing the source of this energy-dependent efficiency change, an empirical approach was adopted, testing various energy-dependent changes to the ion efficiency to determine the approximate variation required to improve the Ni/Ne ratio. These comparisons indicated the sensor was significantly (>40%) more efficient at low energies (<100 eV) then at higher energies (>500 eV). Since ions are pre-accelerated to ~2 keV before striking the MCP, it is unlikely that small variations in initial energy could cause large changes in detector efficiency. Instead we realized that the efficiency change must stem from leakage fields into the electrostatic analyzer from the -2 kV bias voltage on the front of the MCPs. Analyzer simulations had ignored this effect because an exit grid was used to shield the inside of the analyzer.

To quantify the effects of the fringing fields, we used a combination of analyzer simulations and grid transparency corrections. First, a 3-D model of the exit grid and nearby surfaces showed that 2%-3% of the MCP bias voltage would penetrate the grid. Second, the impact of this leakage field was characterized with a 2-D analyzer simulation by replacing the "ideal" exit grid with a potential surface that varied linearly from 40V at the edges to 60 V at the center. The analyzer geometric factor was found to increase by ~30% at low energies due to the fringing fields, with an e-fold drop in this additional sensitivity at ~180 eV. Third, we recognized that a secondary effect of the fringing field would be to focus low energy ions away from the grid wires, increasing the 90% exit grid

transmission to about 100% at low energy. This was also simulated to estimate the exit grid effective transmission as a function of energy. Fourth, a separate "MCP grid" was placed in front of the detector and biased at the MCP voltage to increase detector efficiency. Due to the alignment of a MCP grid with the exit grid, the transmission of the MCP grid could also vary with energy. Simulations showed a complicated transmission function for the MCP grid caused by particle focusing by the exit grid, with some increased transmission at lower energies. Full characterization of this dependence was not attempted and instead an increase from 90% to 95% at low energies was estimated from the simulations. Combining these leakage field effects we obtained a ~45% increase in analyzer geometric factor at low energies. Figure 11c shows the final energy-dependent efficiency correction used for THEMIS ion ESAs, which includes both the fringing field and the MCP detector variations (see Figure 11b).

We point out that a similar energy-dependent analyzer affect is likely present the electron analyzers. It would manifest itself at lower energies since the voltage on the front of the MCPs is only ~450 V. Based on ion sensor simulations, we might expect the enhanced sensitivity to have an e-folding decrease at ~45 eV from the maximum transmission at ~0 eV. In addition, there is a second effect exclusive to electron analyzers. Electrons at energies >50 eV are capable of producing secondary electrons when they strike the outer or inner hemisphere. These low energy secondary electrons will be accelerated to the detector by the fringing fields if the incident particle strikes the hemisphere near the analyzer exit. This additional enhancement in analyzer secondary production kicks in at about the same energy that the enhanced throughput falls off. If the effects are similar in magnitude, it may be that the combined response is relatively flat. To sort out these effects would require a complex analyzer simulation which is beyond current THEMIS data analysis plans. However, after many comparisons between ion and electron densities, we conclude there are no large changes in electron sensor (detector+analyzer) energy efficiency curve at these energies indicating the combination of these two effects has a relatively flat dependence on energy. Therefore the energy efficiency curve shown in Figure 11a was adopted and any energy-dependent sensitivity changes due to fringing fields are assume to be absorbed in the overall geometric factor of the electron sensors.

2.3 Instrument dead time corrections

Corrections for instrument dead-time can be important in regions of high particle count rates such as a high-density magentosheath. For plasma sensors, lost counts due to instrument dead-time result from a combination of electronic and detector dead-time. For THEMIS, electronic dead-time was measured as part of the calibration and determined to be 170 +/-10 ns for all Amptek A121 preamplifiers. Detector dead-time is more difficult to determine. For microchannel plate detectors (MCPs), the dead-time is caused by a decrease in gain at high count rate that results in some events dropping below the preamplifier threshold. The gain drop occurs when the microchannels are unable to completely replenish the charge lost after the previous firing. THEMIS ESAs were fitted with high current MCPs for fast recharging and therefore detector dead-time was not expected to be important unless the particle flux manifests as an intense narrow beam that

is focused on a small portion of the detector. The software assumes a nominal 170 ns dead-time for all detector-preamp combinations.

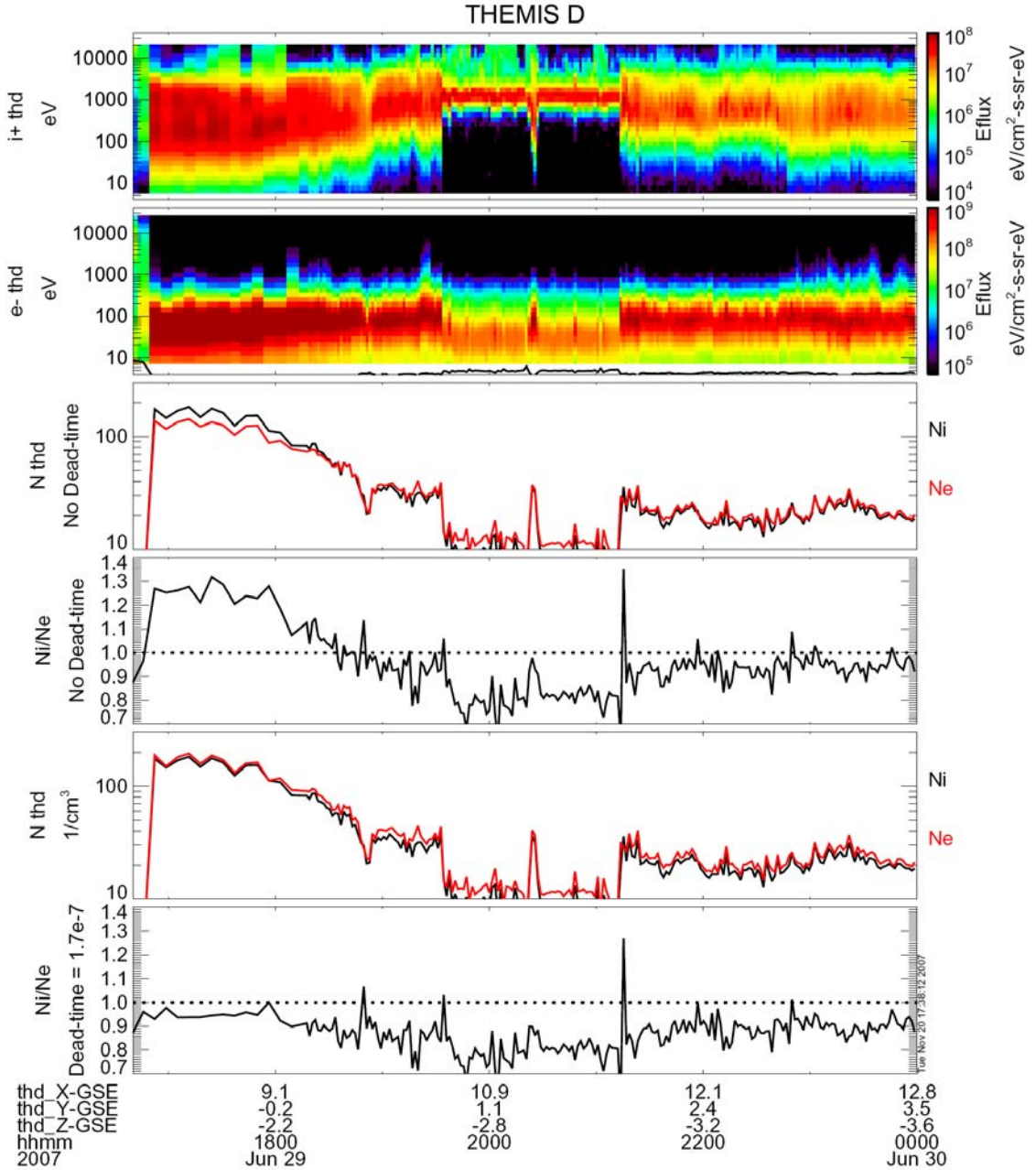

Figure 12: The plot illustrates the importance of dead-time corrections during a day with high magnetosheath density (<19:00 UT). Top panels are ion (panel 1) and electron (panel 2) spectrograms. Panel 3 shows the ion (black) and electron (red) densities uncorrected for dead-time, and panel 4 illustrates how the ratio of these densities results in unphysical 1.0-1.3 values due to underestimation of the electron density. Density ratios should be ~0.9 since solar wind alpha content causes an underestimation of ion density (the calculation assumes protons only). Panel 5 shows the dead-time corrected densities have good agreement and panel 6 illustrates density ratios of ~0.9 as expected. In addition, within the solar wind (19:30-21:20 UT) the ion density is further underestimated due to the narrow beam width.

Nature allowed in-flight testing of our dead-time correction. Figure 12 shows ion and electron data collected during a period of high density magnetosheath plasma. The top panels show ion and electron spectrograms, while panel 3 shows the uncorrected ion and electron densities and panel 4 the ratio of these densities. The electrons require significant dead time corrections prior to 18:30 UT, resulting in a density ratio that exceeds one. Panel 5 shows the dead-time corrected densities and panel 6 confirms an expected ratio of about 0.9 during this period. The reader should ignore the period with un-shocked solar wind (19:30-21:20 UT) where ion densities are underestimated in 32 sweep/spin mode. Figure 12 clearly show that 170 ns dead-time provides a good correction to the data indicating that additional corrections for detector dead-time are less important.

2.4 Calibration of Relative Efficiency with Look Direction

Themis ion and electron ESAs have 16 and 8 discrete anodes, respectively, each of which requires a "relative efficiency" calibration factor to account for small variations in sensitivity with look direction. These relative efficiency corrections are approximately one and do not reflect changes in overall instrument sensitivity. Overall instrument sensitivity is accounted for in the "absolution efficiency" calibration factor discussed in the next section.

For THEMIS electron sensors, the "relative efficiencies" correspond directly to the eight 22.5 degree anodes that cover 180 degrees of polar angle. For ion sensors, which have 16 anodes and up to 5.6 degree resolution, an ideal relative efficiency calibration would result in 16 efficiencies. However, THEMIS data collected in regions useful for calibrations only maintain 22.5 degree resolution. Therefore ion relative efficiencies are determined the same manner as those for electrons. Anodes within a 22.5 degree sector are assumed to have the same relative efficiency as the sector.

THEMIS relative calibrations were accomplished by finding data intervals inside the magnetosphere that met the following criteria:
1. Flows determined by the ion sensor must be small (<30 km/s) and random. This allows us treat the raw data as if it is collected in the plasma frame and ignore pitch angle asymmetries caused by flows.
2. The magnetic field must be relatively constant and make a significant angle (>20^o) with the spin axis. This assures that the same pitch angle is measured by more than one anode during a spacecraft rotation.
3. The average pitch angle distribution of 1-20 keV plasma must be relatively smooth and vary by no more than a factor of 3 (no large anisotropies). This allows us to use a small number of polynomials in the fit and avoid high order terms that tend to reflect statistical fluctuations or beams much narrower than the angle bins. The high energy range (>1 keV) is selected so spacecraft potential variation are unimportant.
4. Data intervals must contain 1-2 hours of Fast Survey data. This criterion assures that 40-75 spins of high angle resolution (88 solid angle) data are available for the fit.

Data between May 31 and August 13 were examined for these criteria, and 10 to 20 intervals were found for each spacecraft. Data from each interval was averaged, sorted by

pitch angle, and fit to a 6th order symmetric polynomial $f= a+bx^2+cx^4+dx^6$, where $x=\cos\theta$ and θ is the pitch angle. Relative efficiencies were calculated by minimizing the variance in the least-squares fit and the fitting algorithm was repeated. This procedure was iterated until efficiencies converged to optimal values for each interval. Figure 13 illustrates the initial and final pitch angle distributions, with different anodes indicated by color and each point a different solid angle. Convergence to the right plot in the figure determines the combined anode and integration time efficiencies. Two anodes (red, magenta) have twice the integration time and two anodes (black) have four times the integration time, which accounts for the majority of the initial difference in the left plot.

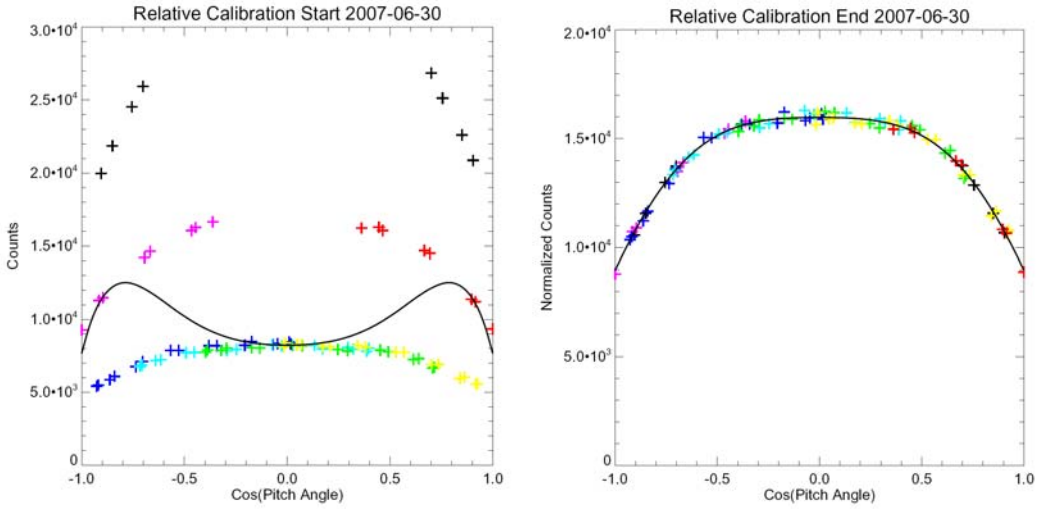

Figure 13: Plots generated as part of the relative anode efficiency calibration algorithm. Different anodes are different colors and each "+" represents a different solid angle bin. The left plot shows the raw counts in each bin as a function of pitch angle. The right plot shows normalized counts after anode efficiencies have been applied. Anode efficiencies are determined through minimum variance to a 6th order symmetric polynomial. Part of the initial large variation in efficiency is due to integration time with two of the anodes (both shown in black) supplying solid angle bins that have 4 times the integration time and two additional anodes (red and magenta) having twice the integration time.

Once efficiencies were calculated for the different intervals, they were averaged and incorporated into the code. Anode efficiencies were generally within about 10% of unity, with the largest variations associated with slightly smaller anodes in the pole channels (which were designed to prevent noise counts near the edge of the microchannel plate detectors). The standard deviation of the relative efficiencies over the intervals was ~1.5% for ions and ~1% for electrons indicating sound methodology and high precision. Since there were no systematic trends in these efficiency variations with time, we assume that these relative efficiencies are constant.

In using a symmetric polynomial to model the pitch angle distribution, we assumed that the distribution was stable and that sufficient bounce-averaging of plasma between magnetic poles had removed any asymmetry in the distribution. This is probably not the case and therefore this assumption may introduce an asymmetric, systematic error to the relative efficiencies. This asymmetry cannot be removed by simply including asymmetric

terms in the pitch angle model. This is because the pitch angle overlap between anodes is generally limited to adjacent anodes so the fitting algorithm does not have a strong constraint on large-angle variations. Any large-angle asymmetry in the input distribution cannot be distinguished from an asymmetry in efficiencies. Therefore we are forced to use other methods to evaluate and correct for asymmetries in the response.

A simple estimate of the magnitude of any asymmetric response can be made by comparing the sensitivity of the two halves of the sensor. Since the sensors are symmetric, with hemispheric concentricity generally better than 1%, the average response of the 0^o to 90^o and 0^o to -90^o sensor halves are expected be very close. Indeed they are found to differ by only ~0.5% for electrons, and by <2% for ions (except for one sensor that differed by ~4%). Ion distributions during quiet periods in the magnetosphere were then checked for systematic flows in the z-direction and no statistically significant flows were found. Since small errors in electron ESA asymmetry can result in large flow errors along the spacecraft spin axis, we compared electron and ion flows in the magnetosheath during July 21-25, 2007. A first order ($\cos\theta$) asymmetry at the 1%-3% level was then introduced to the electron efficiencies to obtain agreement between ion and electron flows. This correction was tested in data from August 21-25, 2007 and found to have good agreement.

2.5 Cross-Calibration of the Sensors

The five electron and five ion ESAs on the THEMIS spacecraft each require a "sensor-level relative efficiency" calibration that accounts for overall variations in efficiency between instruments. These near unity efficiencies will change with time as detectors age and as detector bias voltages are increased to compensate for decreasing detector gains. We chose to separate this relative cross-calibration from an absolute calibration since we had all five satellite data sets in close proximity at the start of the mission and because we lacked a reference for absolute calibration. Since THEMIS does not have a high-frequency measurement of the plasma frequency, absolute calibration will require comparisons with upstream solar wind monitors, such as Wind and ACE, as discussed in the next section.

For this cross-calibration we use the already-determined relative anode efficiencies and energy-dependent detector efficiencies to calculate a sensor-level calibration factor that forces agreement between the separately determined densities. These calibrations cannot be performed in the magnetosphere since it often contains significant cold plasma that is unmeasured. Instead we focus on the magnetosheath where flows are large enough to assure nearly all ions are measured and where spacecraft potential corrections are relatively small. We emphasize that even though the spacecraft potential in the magnetosheath is rather low, typically 5-6 volts, inclusion of the spacecraft potential in the density calculation is critical. For spacecraft whose electric field sensors were not deployed (THA and THB), we used measured potentials from other spacecraft, with corrections as described in section 2.1, to estimate their spacecraft potential. Lastly, since the ion plasma sensor is not mass resolving, we must also account for differences in estimated density between ion and electron sensors due to the presence of alpha particles

in the solar wind. These were accounted for by using upstream solar wind measurements from Wind.

Since THC was the first spacecraft with deployed electric field sensors, early cross-calibration efforts focused on inter-comparisons of its electron and ion sensors. Its observations were used to investigate two months of data (late-May to early-August, 2007) and select a ten days where cross-calibrations would be possible. Selected days had measurements from all spacecraft while in the magnetosheath, and if possible were selected for low alpha content to minimize mass-dependent corrections. Since these are relative calibrations, the electron sensor on THC on June 28, 2007, was selected as a reference, its pre-launch estimated geometric factor used as a baseline, and its efficiency set to one. THC's ion sensor was then cross-calibrated, and its pre-launch geometric factor adjusted to give the same density as the electrons, and its efficiency was set to one. Following these baseline determinations, we set the geometric factors of all other electron and ion sensors to the same values determined above and calculated their sensor-level efficiencies to get agreement between densities. This was accomplished by first cross-calibrating ion and electron sensors on each spacecraft, then cross calibrating electron sensors on each spacecraft with THC's electron sensor.

Figure 14 shows an example of the type of data used to perform the cross-calibration. The top four panels are ion and electron spectrograms and allow quick determination of the various regions: magnetosphere (<12:30 UT), magnetosheath (12:30-17:00 UT) and solar wind (>18:00 UT). Panel 5 shows the density determined from the electron and ion sensors on THC and THD, after the calibration process. As discussed above, ion-electron sensor cross-calibrations on the same spacecraft are performed in the magnetosheath. Panels 6 and 7 show that the Ni/Ne ratios have been matched to ~0.99 during the 12:30-17:00 UT period. (Upstream Wind-3dp plasma data indicated very low alpha content.) The inter-spacecraft cross-calibration is performed between electron sensors in the solar wind (>18:00 UT) as illustrated in panel 8. The variance in the plots results from a combination of counting statistics and temporal variations less than the spin period.

The above calibration procedure was repeated for the 10 selected days. It was then assumed that relative efficiencies of sensors only decreased with time as the detectors aged unless detector bias voltage was increased. This assumption forced a renormalization of the sensor-level efficiencies on each day, except our reference day of June 28, so that each sensor's efficiency monotonically decreased in time. Over the 72 day interval starting 2 months after sensor turnon, sensor efficiency degradation of 10%-15% was estimated by this method. Since random errors in the determination of these detector efficiencies may result in an over estimation of degradation, it may be necessary to correct these calibrations with an overall mission-level efficiency using upstream solar wind measurements.

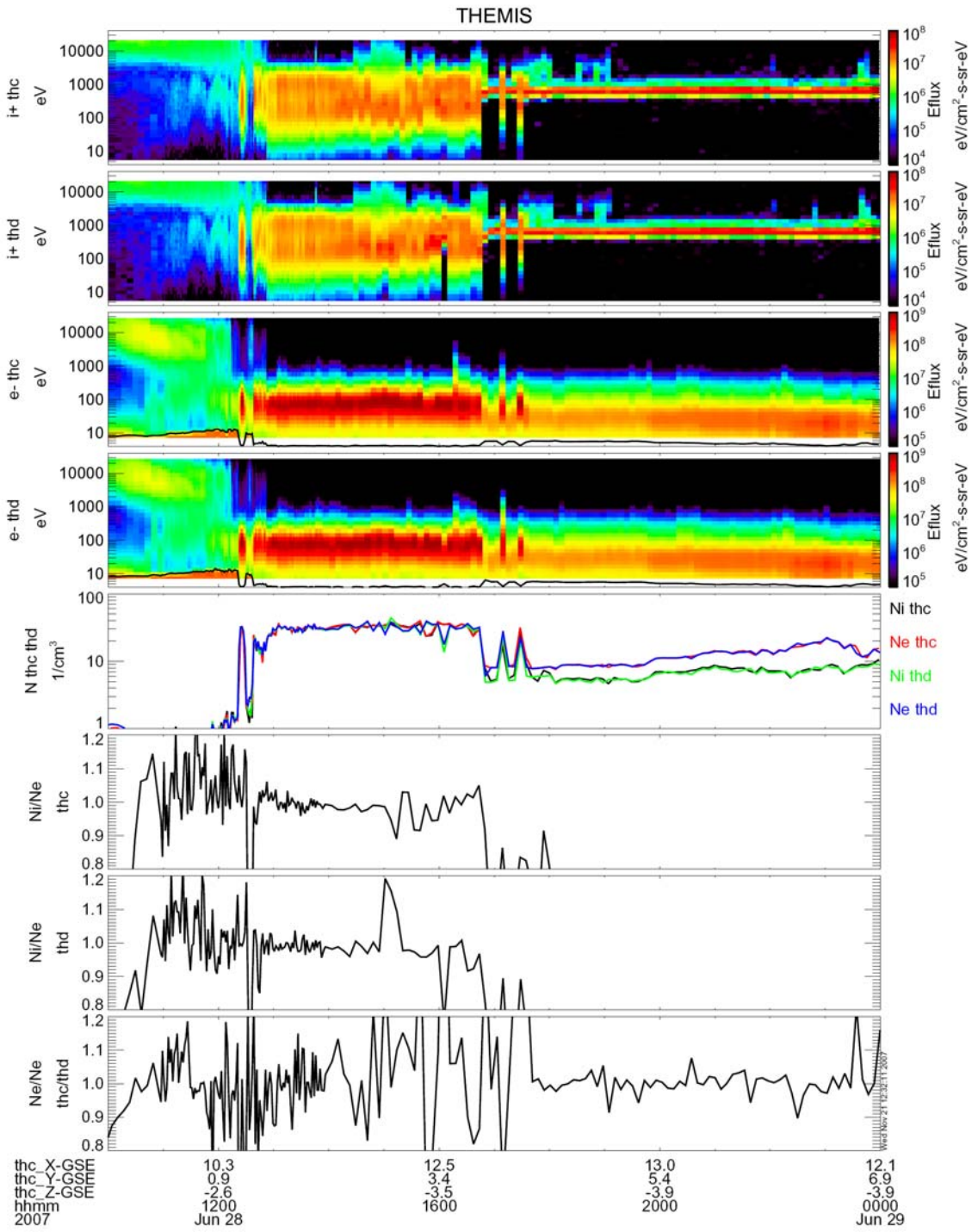

Figure 14: Example of the cross-calibration analysis. Ion-electron sensor cross-calibrations use Ni/Ne ratios measured on the same spacecraft (panel 6,7) within the magnetosheath (12:30-17:00) and match the result to the expected ratio based on upstream alpha content, ~0.99 in this case. Inter-spacecraft cross-calibrations match electron densities within the solar wind (>18:00 UT) as illustrated in panel 8. Solar wind ion densities are underestimated due to the narrow solar wind beam and therefore not used in calibrations.

2.6 Absolute Calibrations

The calibration efforts described above resulted in a consistent set of relative calibrations between measurements within a sensor, and consistent measurements between different sensors. However, there is no test in the above procedures that determine the absolute sensitivity of the sensors. All measurements of the even moments, such as density and pressure, or measurements of flux and energy flux, which are proportional to density, will be incorrect by some scale factor. For these calculations, the absolute sensitivity, or absolute geometric factor plus efficiency, was estimated from a combination of analyzer simulation and estimated detector efficiencies. To determine this absolute calibration will require a comparison of the THEMIS ESA response to a known "standard candle" plasma parameter. Generally this standard candle is the plasma frequency which determines the electron density. However since THEMIS spacecraft do not have high frequency wave receivers, absolute calibration will have to be determined through comparisons with other spacecraft. Since the THEMIS spacecraft are rarely near any other magnetospheric spacecraft for cross-calibrations and since magnetospheric plasma regimes vary dramatically in density and pressure, the most favorable location for consistent cross-calibrations is the solar wind.

Absolute sensitivity of the plasma sensors was tested through cross-calibration with the Wind-SWE instrument (Ogilvie et al., 1995). Electron densities measured by THEMIS THC and THD in the solar wind were compared with SWE proton densities, with appropriate corrections for time delays based on the location of the Wind spacecraft. Five intervals during a two month period were compared and a 0.7 correction to the THEMIS densities was required to give good agreement. Figure 15 shows an example of this cross-calibration. The top panels show the THC and THD electron spectrograms with nearly identical solar wind plasma. The black lines indicate spacecraft potential, $e\Phi_{sc}$. The third panel shows the IMF magnitude (Wind-black, THC-red, and THD-green) which is assists in determination of the temporal alignment and verification of the suitability of the time interval. The bottom panel demonstrates that the Wind-SWE, THC and THD densities have good agreement after the correction factor is applied. Since $e\Phi_{sc}$ was below the lower energy cutoff of the THEMIS electron sensors, this comparison used a density calculation algorithm that extrapolated the distribution function to $e\Phi_{sc}$, assuming a Maxwellian distribution. For the data in Figure 15, this algorithm introduced a 2% to 9% increase in the calculated the THEMIS electron density relative to a simple algorithm that just used the measured energy range.

The above cross-calibration indicates the THEMIS electron ESA pre-flight geometric factors were underestimated. Recall in section 2.5, the ion sensor geometric factor were adjusted to provide good agreement in the electron-ion cross calibration, therefore the ion sensors required similar scaling by the correction factor. For the five intervals tested, the correction factor was relatively constant and showed no systematic change in time. Temporal variations between the measurements indicate that errors in this cross-calibration are at the ~10% level. This correction factor was combined with the pre-flight sensor geometric factors to obtain the absolute sensor geometric factors.

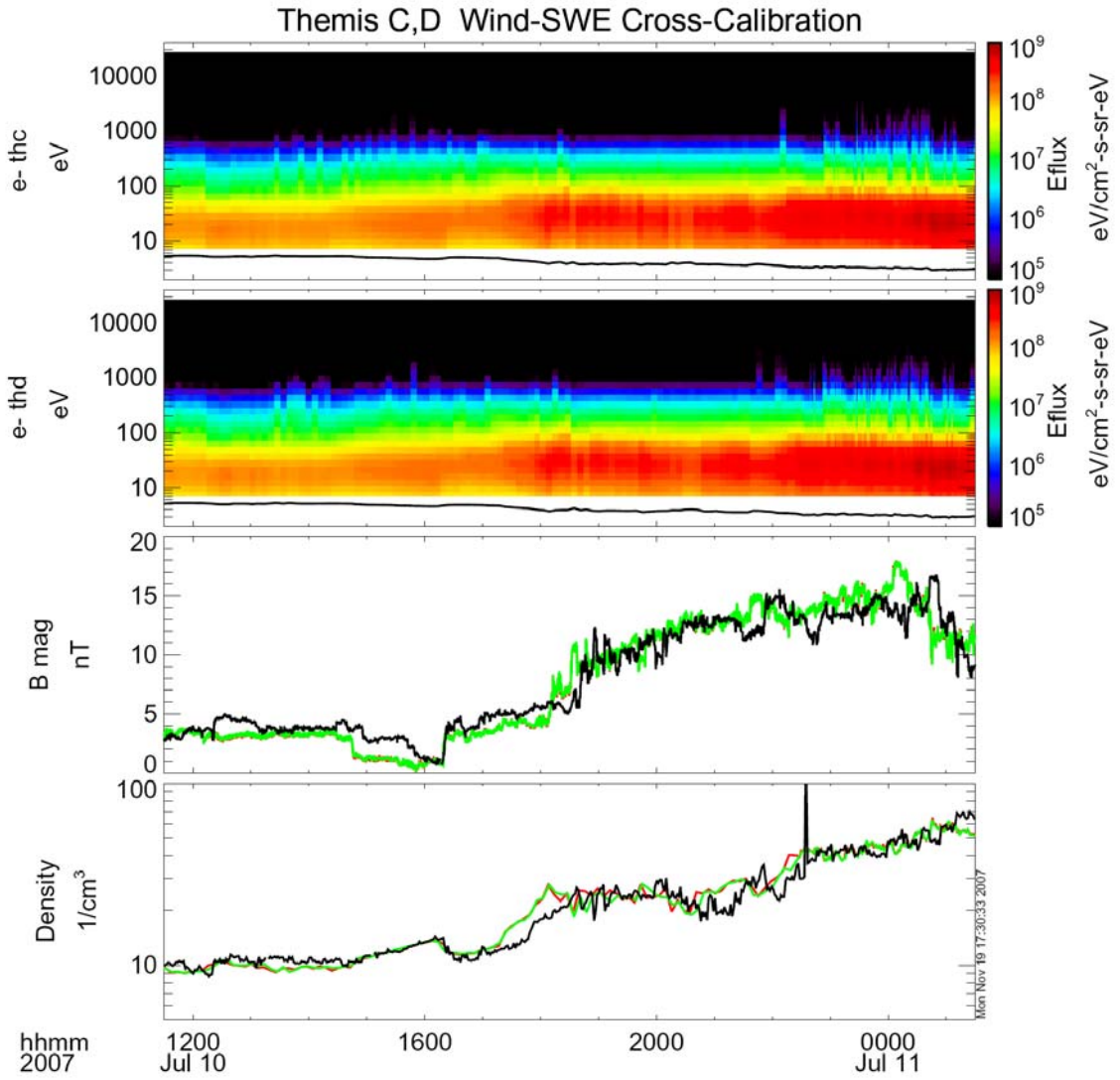

Figure 15: Plot illustrates the cross calibration between Wind-SWE and THEMIS electron ESAs used to determine absolute sensitivity. The plot shows electron spectrograms from THC (panel 1) and THD (panel 2) in the solar wind. Panel 3 shows the IMF magnitude on Wind (black), THC (red) and THD (green). Panel 4 shows the agreement between ion density on Wind (black), and electron density on THC (red) and THD (green) after the cross calibration.

As a final test of the absolute calibration, magnetopause crossings were evaluated to check for pressure balance. Figure 16 shows an example that contains several magnetopause crossings in addition to flux transfer events. The bottom panel shows the electron (red), ion (green), and magnetic (blue) pressures, in addition to the combined pressure (black). The nearly constant total pressure during these crossings indicates accurate absolute calibrations.

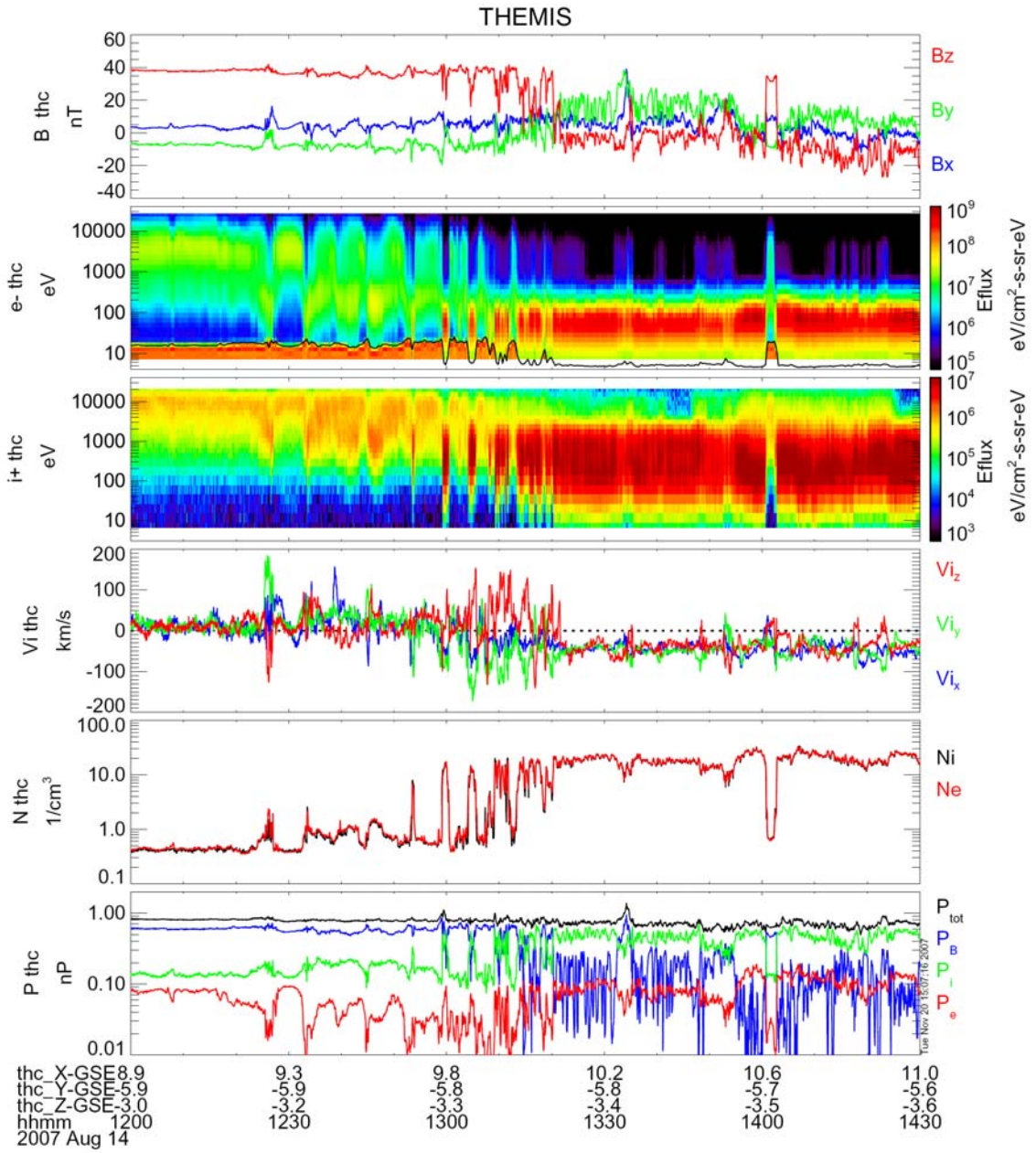

Figure 16: THEMIS magnetopause crossing used to test calibrations. From top to bottom: magnetic field, electron spectrogram, ion spectrogram, ion velocity, density, and pressure. Good agreement of the electron (red) and ion (black) densities (panel 5) indicates good cross-calibration. Nearly uniform pressure across several magnetopause boundaries, across several flux transfer events, and within magnetosheath mirror modes, reveals accurate absolute calibrations.

3.0 Summary

The THEMIS ESA plasma instrument measures the 3-D distribution functions of electrons (up to 30 keV) and ions (up to 25 keV) using a pair of "top hat" electrostatic analyzers. Particle events identified by microchannel plate detectors are binned into six distributions whose energy, angle, and time resolution depend upon instrument mode. Omni-directional spectra or coarse-angle resolution distributions are continuously available at spin resolution (3 s). Higher energy-angle resolution distributions are available at a lower cadence or at spin resolution during burst data collection. In addition, on-board data processing generates plasma moments at spin resolution that include corrections for spacecraft charging.

The overall design of the THEMIS ESA plasma instrument was directly derived from the FAST Plasma Instrument (Carlson et al., 2001). This modular design simplified assembly and subsystem testing of the 10 flight ESAs. The primary changes from the FAST design were the development of a reset-able closing mechanism that utilizes an SMA actuator to seal the detector from contamination, and the change from gold-black to ebanol-C blacking which reduces scattered sunlight from reaching the detector. Ground calibrations showed the five sensor pairs to be nearly identical in response and all ten sensors continue to perform optimally after 10 months.

The close proximity of the THEMIS satellites during the first 7 months of the mission allowed extremely accurate multi-satellite cross-calibrations of the plasma sensors. These calibrations were facilitated by having all the plasma measurements available with the same resolution and format, along with spacecraft potential and magnetic field measurements in the same data set. The methodology of the in-flight calibration effort has been outlined in this paper, and its precision demonstrated through comparisons with Wind-SWE and total pressure across the magnetopause. However, this calibration effort is not complete. The THEMIS plasma instruments will require monitoring throughout the mission to track and quantify degradation of the MCP detectors and to determine the adjustments to their bias voltages. Future tracking and calibration efforts will utilize the same methods employed above, but will be more difficult due to larger spacecraft separations. It is envisioned that additional cross-calibration efforts will rely on the few month period each summer when multiple satellites encounter the solar wind. Lessons learned from this effort should be useful for future multi-satellite missions.

Acknowledgements

This research was supported by NASA fund …

References

U. Auster, K.-H. Glassmeier, et al., Space Sci. Rev., this issue, 2008.

J.W. Bonnell, F.S. Mozer, G.T. Delory, A.J. Hull, R.E. Ergun, C.M. Cully, Space Sci. Rev., this issue, 2008.

C.W. Carlson, D.W. Curtis, G. Paschmann, and W. Michael, Adv. Space Res., **2**, 67-70, 1983.

C.W. Carlson, J.P. McFadden, P. Turin, D.W. Curtis, A. Magoncelli, Space Sci. Rev., 98, p.33-66, 2001.

R.R. Goruganthu, W.G. Wilson, Rev. Sci. Instrum., **55**(12), 2030, 1984.

R.S. Gao, P. S. Gibner, J. H. Newman, K. A. Smith, and R. F. Stebbings, Rev. Sci. Instrum., **55**(11), 1756, 1984.

P.R. Harvey, et al., Space Sci. Rev., this issue, 2008.

D. Larson, T. Moreau, R. Lee, R. Canario, and R. P. Lin, Space Sci. Rev., this issue, 2008.

J.P. McFadden, C.W. Carlson, D. Larson, V. Angelopolos, Space Sci. Rev., this issue, 2008.

J.P. McFadden et al., in Calibration of Particle Instruments in Space Physic, ed. by M. Wuest, D. Evans and R. von Steiger, (ISSI Publication, Bern, Switzerland, 2007), p. 285

Ogilvie, K. W., D. J. Chorney, R. J. Fitzenreiter, F. Hunsaker, J. Keller, J. Lobell, G. Miller, J. D. Scudder, E. C. Sittler Jr., R. B. Torbert, D. Bodet, G. Needell, A. J. Lazarus, J. T. Steinberg, J. H. Tappan, A. Mavretic, and E. Gergin, Space Sci. Rev., 71, 55-77, 1995.

Straub, H. C., M. A. Mangan, B. G. Lindsay, K. A. Smith, and R. F. Stebbings, Rev. Sci. Instrum., 70(11), 4238, 1999.

Taylor, E., et al., Space Sci. Rev., this issue, 2008.

Vassilis, A. et al., Space Sci. Rev., this issue, 2008.